Measurement And Application Of Influence Coefficients For Modeling Nonuniform Electrical Behavior

Author(s): J. K. Koester and R. D. Schlueter

Session Name: Open Cycle II

SEAM: 19 (1981)

SEAM EDX URL: https://edx.netl.doe.gov/dataset/seam-19

EDX Paper ID: 848

MEASUREMENT AND APPLICATION OF INFLUENCE COEFFICIENTS FOR MODELING NONUNIFORM ELECTRICAL BEHAVIOR*

J. K. Koester and R. D. Schlueter
High Temperature Gasdynamics Laboratory
Stanford University
Stanford, California 94305

Abstract

Electrical nonuniformities in MHD generators were studied experimentally and analytically by the technique of "influence coefficients". These coefficients were measured by an AC instrument in both clean fuel and slagging channels. Leakage current effects were studied by applying external shorting resistors and by measuring the polarization time constant for slag layer axial conductance.

A model for nonuniform behavior of arc-mode channels with up to fifty-one electrode pairs was solved numerically using the influence coefficient technique. Buckling type instabilities of electrical axial distributions were observed for sufficiently negative arc dynamic resistance coupled with small external resistive loads. The maximum fault power of an axial short was found to depend on the uniformity of the Faraday current distribution; the trends of the computed variation of fault power were confirmed by nonuniform loading experiments.

I. Introduction

Nonuniformities in electrode currents and voltages occur in MHD generators due to both internal faults and to external circuits. A variety of internal effects such as interelectrode leakage due to surface deposits, Hall voltage breakdown, and arc mode current transport can cause electrical nonuniformities. Although the precise cause of these nonuniformities is often uncertain, they have been observed in both segmented Faraday and diagonal wall generators operating under both slagging conditions as well as with clean fuels.[1,2,3] The recent application of external power conditioning and control circuits results in imposed electrical nonuniformities at frequencies up to a few thousand Hertz. Voltage consolidation circuits require a periodic shuffling of electrode currents at a frequency of a few hundred Hertz.[4] More recently, the role of power conditioning equipment, such as voltage consolidators and inverters, has been expanded to include the control of various internal faults that can arise.

The characteristics of electrical nonuniformities will be described in this paper. The general approach is based on the concept of "influence coefficients" which we described in reference 1. The use of influence coefficients allows the rapid computation of various external circuits interacting through the plasma via a large number of electrode terminals. This technique was employed in a stability study of the arc mode, segmented Faraday generator in which up to 51 electrode pairs were used.

An AC instrument, which can measure influence coefficients during generator operation, has been developed and used to measure these coefficients in three different generator test sections in our laboratory.

The previous experimental work[1] on influence coefficients has been expanded to include the effect of leakage currents by introducing external resistors between adjacent cathodes and/or anodes. The data from these experiments allow both the experimental determination of the influence coefficients for leakage currents while also verifying the usefulness of this technique for predicting nonuniformities due to leakage currents.

Work on the prediction of influence coefficients in the presence of plasma boundary layers has been initiated with the goal of directly comparing these theoretical values with the above measured values.

II. Modeling of Nonuniform Electrical Behavior

The effects of finite segmentation, nonlinear voltage drop, and leakage resistances on the temporal evolution of electrical nonuniformities are modeled by grafting the influence coefficient model for the plasma region to a model for electrode arcs at some appropriate boundary as indicated schematically by the dashed lines in Fig. 1.

Description of the Plasma Region

The Faraday and Hall voltages ($V^P_{Fk}, V^{Pa}_{Hk}, V^{Pc}_{Hk}$) at the edge of the plasma region adjacent to the k-th electrode pair are determined for nonuniform operation by a superposition over all Faraday and leakage currents times their appropriate "influence" coefficient.[1] The k-th Faraday voltage is:

$$V^P_{Fk} = \bar{u}Bh' - R_{ch} \sum_{\text{all } n} (\bar{Z}^{FF}_{k-n} I_n + \bar{Z}^{FA}_{k-n} i^a_n + \bar{Z}^{FC}_{k-n} i^c_n) - \frac{\beta}{w\sigma} \left[\frac{i^a_{k-1} + i^a_k + i^c_{k-1} + i^c_k}{2}\right] \quad (1)$$

where $\bar{Z}^{FF}_{k-n}$, $\bar{Z}^{FA}_{k-n}$, and $\bar{Z}^{FC}_{k-n}$ are the dimensionless influence coefficients for the k-th Faraday voltage due to, respectively, the n-th Faraday, anode leakage, and cathode leakage currents; $R_{ch} \equiv h'/pw\sigma$ is the characteristic plasma resistance, σ is the plasma electrical conductivity, and β is the Hall parameter. The k-th plasma Hall voltage at the anode is given by:

*Supported by the Electric Power Research Institute, Contract RP 468-3.

$$V_{Hk}^{Pa} = \frac{\beta}{w\sigma}\left[\frac{I_k + I_k - i_{k-1}^a + i_{k+1}^a}{2}\right]$$
$$+ R_{ch} \sum_{\text{all } n} (\bar{Z}_{k-n}^{AF} I_n + \bar{Z}_{k-n}^{AA} i_n^a + \bar{Z}_{k-n}^{AC} i_n^c) \tag{2}$$

where $\bar{Z}_{k-n}^{AF}$, $\bar{Z}_{k-n}^{AA}$, and $\bar{Z}_{k-n}^{AC}$ are the dimensionless influence coefficients for the k-th anode Hall voltage due to, respectively, the n-th Faraday, anode leakage, and cathode leakage currents. Similarly, the k-th plasma Hall voltage at the cathode is:

$$V_{Hk}^{Pc} = \frac{\beta}{w\sigma}\left[\frac{I_k + I_{k+1} + i_{k-1}^c - i_{k+1}^c}{2}\right]$$
$$+ R_{ch} \sum_{\text{all } n} (\bar{Z}_{k-n}^{CF} I_n + \bar{Z}_{k-n}^{CA} i_n^a + \bar{Z}_{k-n}^{CC} i_n^c) \tag{3}$$

where $\bar{Z}_{k-n}^{CF}$, $\bar{Z}_{k-n}^{CA}$, and $\bar{Z}_{k-n}^{CC}$ are the dimensionless influence coefficients for the k-th cathode Hall voltage due to, respectively, the n-th Faraday, anode leakage, and cathode leakage currents. These dimensionless influence coefficients are functions of geometry and Hall parameter.

The $\bar{Z}_{k-n}^{FF}$ coefficients can be readily found for the consant conductivity, narrow electrode ($c/p \ll 1$) case by utilizing the plasma kernel (at $\theta = 0$) derived by Solbes and Lowenstein[3] for an infinitely segmented channel:

$$K(\bar{x}) = \ln\left[\frac{\cosh(\pi\bar{x}) + 1}{\cosh(\pi\bar{x}) - 1}\right] \tag{4}$$

where $\bar{x} \equiv (x - x')/h'$. The transverse coefficients are given approximately from the plasma kernel by:

$$\bar{Z}_{k-n}^{FF} \simeq \frac{p}{h'\pi} K\{(k-n)p/h'\} \tag{5}$$

The singularity at $\bar{x} = 0$ can be circumvented by averaging the kernel over the electrode length, c:

$$\bar{Z}_0^{FF} = (p/h'\pi)\langle K\rangle \tag{6}$$

where $\langle K\rangle \equiv \frac{2h'}{c} \lim_{\varepsilon\to 0} \int_{\varepsilon}^{c/2h'} K(\bar{x})d\bar{x}$.

Values of $\bar{Z}_{k-n}^{FF}$ calculated by the kernel method compare favorably (see Table 1) with the previous Laplacian solution;[1] for reference, values for the other influence coefficients and symmetry and reciprocity relationships between the coefficients are included in Table 1.

Application to Arc Mode Generators

The negative voltage-current characteristic of electrode arcs can result in electrical nonuniformities as shown by the linearized stability analysis of Solbes and Lowenstein[5] and the nonlinear analysis of Kuo, et al.[6] The development of these nonuniformities in finitely segmented channels with nonlinear voltage drops is studied here by numerically solving the circuit equations for the model shown by Fig. 1. For the case without leakage resistances, the circuit equation for the k-th electrode pair is:

$$L \frac{dI_k}{dt} + R_{Lk} I_k + \sum_{n=1}^{N} Z_{k-n}^{FF} I_n + V_{arc} = \bar{u} B h \tag{7}$$

where L = circuit inductance, R_{Lk} is the k-th load resistance, and V_{arc} is the sum of the k-th anode and cathode voltage drops. For the present study, V_{arc} is modeled by a linear region followed by an inverse power function of current (see Fig. 2):

$$V_{arc} = D/I^m \quad \text{for} \quad I > I_{crit} \tag{8}$$

Equation (7) represents a coupled set of N nonlinear equations for the N load currents, $I_k(t)$. These equations have been solved for conditions similar to the experimental conditions of a test with the 19 electrode pair, slagging SEG channel in which strong electrical nonuniformities were observed for loads of 13 ohms and less.[1] The calculated response at a loading of 48 ohms due to a single current perturbation is shown in Fig. 3. In about 100 τ (where $\tau \equiv L/R_{ch}$), the perturbation damps out while the end currents increase to a steady state distribution. The behavior at small load resistance is shown in Fig. 4 for R_{Lk} = 1.7 ohms. In this case, the perturbation grows and spreads throughout the channel such that every other electrode pair carries a large current whereas their neighbors are barely conducting. This buckling type of instability is a function of the load, R_L, and the voltage drop parameters D, m, and I_{crit}, as well as geometry. A stability map in terms of R_L and D is presented in Fig. 5 for m = 1/4. The region of instability occurs for sufficiently low load resistance and high voltage drop level. These results are compared with the linear stability result of

Table 1

Influence Coefficients for Constant Conductivity Case: p/h = 0.156, c/h = 0.010

k-n	Analytical $\bar{Z}_{k-n}^{FF}$	Previous Solution[1] $\bar{Z}_{k-n}^{FF}$	$\bar{Z}_{k-n}^{CF}$	$\bar{Z}_{k-n}^{CA}$	$\bar{Z}_{k-n}^{CC}$
-3	.037	.040	-.014		+.004
-2	.062	.069	-.030	-.002	+.013
-1	.113	.13	-.174	-.003	+.14
0	.461	.47	.174	-.003	-.35
1	.113	.13	.030	-.003	+.14
2	.062	.069	.014	-.002	+0.13
3	.037	.040	.008		+.004
4	.02	.024	.005		+.002
5	.014	.014	.003		+.001
6	.008	.009	.001		

Note
$$\bar{Z}_{k-n}^{FC} = -\bar{Z}_{k-n}^{FA} = -Z_{k-n-1}^{CF} = Z_{k-n-1}^{AF}$$
$$\bar{Z}_{k-n}^{CC} = \bar{Z}_{k-n}^{AA}$$
$$\bar{Z}_{k-n}^{AC} = \bar{Z}_{k-n}^{CA}$$

reference 5 in which the most unstable wavelength occurs at 1.7 p:

$$R_L + \frac{d\,V_{arc}}{dI} > \frac{1.7}{\pi} R_{ch} \frac{p}{h} \quad \text{for stability} \qquad (9)$$

As shown by Fig. 5, the linearized analysis applied locally overpredicts the region of instability.

The experimentally observed instability corresponds to a value of D = 194 on Fig. 5, which is consistent with measured voltage drops in the range of 150-200 volts.

Effect of Leakage Currents. The incorporation of leakage currents in the model requires two additional axial circuit equations and separate models for the arc voltage drop at the anode and at the cathode. The complete set of circuit equations for the model shown by Fig. 1 is:

$$V^P_{Fk} = L\frac{dI_k}{dt} + R_{Lk} I_k + V^a_{arc_k} \; V^c_{arc_k} \qquad (10)$$

$$V^{Pa}_{Hk} = R^a_k i^a_k - V^a_{arc_{k+1}} + V^a_{arc\ k} \qquad (11)$$

$$V^{Pc}_{Hk} = R^c_k i^c_k + V^c_{arc_{k+1}} - V^c_{arc_k} \qquad (12)$$

where R^a_k and R^c_k are the effective anode and cathode leakage resistances between the k-th and (k+1)-th anode and cathodes, respectively. The plasma voltages (V^P_{Fk}, V^{Pa}_{Hk}, and V^{Pc}_{Hc}) are related to the Faraday and leakage currents by Eqs. (1) to (3). The voltage drops are related to the currents by:

$$\begin{aligned} V^c_{arc_k} &= V^a_{arc_k}\,(I_k - i^a_{k-1} + i^a_k) \\ V^c_{arc_k} &= V^c_{arc_k}\,(I_k + i^c_{k-1} - i^c_k) \end{aligned} \qquad (13)$$

An N-electrode pair channel is described by the 3N-2 equations (Eqs. (10), (11), (12)) along with N initial conditions for the Faraday currents. The temporal evolution of the Faraday and leakage currents and voltages are found as a function of the load and leakage resistances.

The coupled 3N-2 nonlinear equations are solved numerically for $dI_k(t)/dt$, $i^a_\ell(t)$, and $i^e_\ell(t)$ (K=1,...N), (ℓ=1,...N-1), using a Newton-Raphson method whereby a Jacobian matrix of the partial derivatives with respect to dI_k/dt, i^a_ℓ and i^c_ℓ (k=1,...N), (ℓ=1,...N-1) is used to drive residuals to zero by iterating. Values of the above 3N-2 time dependent variables from the preceeding time step are used as initial guesses for the current time step. After all dI_k/dt's and leakage currents have converged (typically after 2 to 10 iterations) to within some small ε, a forward Euler method is used to calculate the values of the Faraday currents for the next time step.

The electrical response of anode insulator breakdown and of cathode/anode polarization are readily simulated through the manipulation of the leakage resistances and by using appropriate voltage drop models at the anode and at the cathode.

Typical Results

Leakage currents play an important role in the development of buckling type instbilities. Using a negative arc voltage characteristic of $V = ae^{-bI}$ smoothly grafted into a linear region at low currents (Fig. 6) the effect of leakage on the temporal evolution of the Faraday currents was studied for several external loads. For large external loads, leakage currents typically lead to small nonuniformities of the Faraday currents (Fig. 7), while for small loads leakage currents greatly affect the magnitude, distribution, and temporal evolution of the Faraday currents. Figs. 7 and 8 show that an anode leakage current tends to augment the upstream Faraday current, as expected from the Hall effect. In Fig. 8 for the case without leakage the buckling instabilities propagate inward from the ends, while for the case with leakage the instabilities originate at the center, resulting in a different final Faraday distribution.

Initial current perturbations also have a large effect on instability propagation due to the nonlinear behavior of the arc voltage drop. Figure 9 shows two cases where buckling type instabilities propagate outward from initial current perturbations resulting in different Faraday current distributions. When instabilities arise the preferred mode is a high-low-high-low Faraday current distribution, however numerous other modes (e.g., high-high-low-low) have been observed for different initial current perturbations and leakage currents.

III. Channel Experiments

Loading experiments were conducted with both the clean fuel M-2 facility and the slagging SEG flowtrain. Influence coefficients were measured for three channels: the M-2, SEG, and PEG, a small, high magnetic field channel. The characteristics of these three channels are summarized in Table 2.

Table 2

Test Channel Characteristics

Channel	Fuel	# Electrodes	w x h cm^2	p/h	B (T)
M-2	Ethanol	13	3.2x10.2	0.375	1.8
PEG	Ethanol	26	1.4x 6.2	0.081	5.0
SEG	Coal Slurry	19	3.2x10.2	0.156	2.6

The M-2 facility consists of the M-2 combustor (which operates on ethanol and oxygen), a run-in section, and the thirteen electrode pair M-2 test section. The flow area is h x w = 10.2 x 3.2 cm^2; pitch-to-height ratio p/h = .38 and electrode length-to-pitch ratio c/p = 0.5. The channel sidewalls were ~2000 K magnesia and the electrodes were ~1300 K stainless steel. The mass flow rate was 0.16 kg/sec with $N_2/O_2 = 0.5$.

Slagging Flowtrain

The slagging generator flowtrain is shown in Fig. 10. The M-8 combustor is fired on a pulverized coal/ethanol slurry with oxygen and has a residence time of 20-40 msec. The combustor is followed by a subsonic nozzle, three run-in sections, the generator test section, a diagnostic section, and a diffuser.

The generator test section consists of nineteen electrode pairs with a pitch-to-height ratio of 0.16, an electrode length-to-pitch ratio of 0.8, and insulating sidewalls of a metal pegwall design. The flow area is 3.2 x 10.2 cm^2. Electrodes No. 5 through 10 were stainless steel operating at about 1200 K; the other electrodes were ~500 K platinum clad copper.

Instrumentation. The generator test section was fitted with iridium voltage probes in the sidewall. Thermocouples were installed in each electrode cap and in each electrode base. Pressure taps were located at seven ports throughout the flowtrain. Reactant flowrates were monitored by rotameters and/or digital swirlmeters. Current shunts were used on all nineteen top electrodes and bottom electrodes. All current shunts and electrode thermocouples were isolated from high common mode voltage by optical isolators. Faraday, Hall and probe voltage signals were read through voltage dividers.

All electrical and most flow data were scanned, digitized, reduced, recorded, and displayed by a computer controlled data acquisition system consisting of an HP2100 minicomputer, Vidar scanner and IDVM, system console, line printer and video monitors.

Continuous recording of critical parameters was made on an eight-channel strip chart recorder. The time dependent behavior of electrode currents, voltage drops, Hall voltages, and probe voltages were obtained by using a fourteen-track analog tape recorder. Slag surface temperature was measured with an optical pyrometer.

Test Conditions. Test SEG-13 was carried out with Illinois #6 coal. The flow conditions were: mass flowrate = 0.23 kg/sec, $N_2/O_2 = 0.25$, fuel rich equivalence ratio = 1.1, ash mass fraction = 0.35 percent, and seed mass fraction = 1.0 percent.

Measurements of Influence Coefficients

The development of an AC instrument has allowed the in situ measurement of influence coefficients for several generator test sections. The effect of frequency on plasma conductivity can be determined by adding the term $1/\nu_{eH}\ \partial\vec{J}/\partial t$ to $\vec{J}$ in the generalized Ohm's law[7] where ν_{eH} is the electron collision frequency. This extra term is negligible at frequencies much less than $F_{crit} = \nu_{eH}/2\pi$. For combustion plasmas, F_{crit} is typically 40,000 MHz so that even at frequencies of several MHz, the plasma conductivity and hence current distributions in the plasma are the same as for the DC case. However, the AC voltage drop at the electrodes is quite different in the arc mode since the dynamic impedance of the arcs is small and even negative for cold electrodes. The use of AC probing currents provides a powerful technique for monitoring the resistance of internal generator insulator elements and for inferring information about current distribution in the plasma. For various practical reasons, AC diagnostics have been developed in the frequency range of 20-40 kHz; this frequency range is low enough that the effects of stray capacitance and lead inductance are minimized, yet high enough that noise due to lower frequency (0-10 kHz) inherent fluctuations is eliminated.

The AC influence coefficient instrument is shown schematically in Fig. 11. An AC current is applied through 1 μF blocking capacitors to the n-th electrode pair. The "influence" of the AC current is determined by measuring the AC voltage signal at neighboring electrode pairs. These AC current and voltage signals are processed with bandpass filters, then rectified and divided to produce a quantity (such as $R^{FF}_{k-n} \equiv |\tilde{V}_{Fk}|/|I_n|$ in Fig. 11) which can be related to influence coefficients. Since all phase information is lost in the rectification process, the signs of the influence coefficients are determined from the analytical work; the appropriate signs are summarized in Table 3.

Table 3

Listing of Signs for Influence Coefficients

ℓ	Z^{FF}_ℓ	Z^{FA}_ℓ	Z^{FC}_ℓ	Z^{AF}_ℓ	Z^{CF}_ℓ	Z^{AA}_ℓ Z^{CC}_ℓ	Z^{AC}_ℓ Z^{CA}_ℓ
-2	+	-	+	+	-	+	-
-1	+	-	+	+	-	+	-
0	+	-	+	-	+	-	-
1	+	+	-	-	+	+	-
2	+	+	-	-	+	+	-

Since the AC current is applied as a single Faraday or leakage current, the plasma voltage equations (Eqs. (1)-(3)) can be readily inverted in terms of a single influence coefficient. Three types of influence coefficients are directly related to the measured quantity: $Z^{FF}_\ell = R^{FF}_\ell$, $Z^{AC}_\ell = -R^{AC}_\ell$, and $Z^{CA}_\ell = -R^{CA}_\ell$. The others involved the additional parameters $\alpha \equiv \beta/w\sigma$ near $\ell = 0$. These relationships are summarized below for anodes:

$$\begin{aligned} Z^{AF}_{-2} &= R^{AF}_{-2} \\ Z^{AF}_{-1} + \tfrac{1}{2}\,\alpha &= \pm\, R^{AF}_{-1} \\ Z^{AF}_{0} + \tfrac{1}{2}\,\alpha &= \mp\, R^{AF}_{0} \\ Z_{1} &= -R^{AF}_{1} \end{aligned} \tag{14}$$

- -

$$\begin{aligned} Z^{FA}_{-1} &= -\, R^{FA}_{-1} \\ Z^{FA}_{0} + \tfrac{1}{2}\,\alpha &= \mp\, R^{FA}_{0} \\ Z^{FA}_{1} + \tfrac{1}{2}\,\alpha &= R^{FA}_{1} \\ Z^{FA}_{2} &= R^{FA}_{2} \end{aligned} \tag{15}$$

- -

$$\begin{aligned} Z^{AA}_{-2} &= R^{AA}_{-2} \\ Z^{AA}_{-1} - \tfrac{1}{2}\,\alpha &= \pm\, R^{AA}_{-1} \\ Z^{AA}_{0} &= -\, R^{AA}_{0} \\ Z^{AA}_{1} + \tfrac{1}{2}\,\alpha &= R^{AA}_{1} \\ Z^{AA}_{2} &= R^{AA}_{2} \end{aligned} \tag{16}$$

where the upper sign is the most likely for agreement with Table 3. A similar set of equations can be readily written for the cathode related influence coefficients. The application of the above relationships is subject to two conditions: first, that the AC current is flowing only through the plasma and second, that the AC voltage drops are negligible. The first condition can be met by setting all external loads much larger than the plasma resistance. The second condition is more nearly attained in slagging, cold electrode channels operating with DC currents.

The transverse influence coefficients due to Faraday current, Z^{FF}_{ℓ}, were measured for three channels with widely different pitch-to-height ratios. The effect of plasma conductivity variations was eliminated by comparing values normalized by the plasma resistance, R_p, for a uniformly operating channel:

$$\hat{Z}^{FF}_{\ell} = Z^{FF}_{\ell}/R_p \tag{17}$$

Note that $\sum_{-\infty}^{\infty} \hat{Z}^{FF}_{\ell} = 1$, which provides a method for directly eliminating R_p. The measured coefficients are shown in Fig. 12 as a function of pitch-to-height ratio. Note that the zeroth coefficient approaches a value of unity for large pitch-to-height ratio, whereas the higher order coefficients exhibit a maxima.

These measured values are compared in Fig. 12 with the constant conductivity analytical results described in Section II. The relationship between the experimental normalized influence coefficients given by Eq. (17) and those derived analytically (Eq. (5)) is:

$$\hat{Z}^{FF}_{\ell} = \bar{Z}^{FF}_{\ell} \Big/ \sum_{-\infty}^{\infty} \bar{Z}^{FF}_{\ell}$$

where $\sum_{-\infty}^{\infty} \bar{Z}^{FF}_{\ell}$ is greater than one due to current constrictions. The agreement with the constant conductivity solution is better than expected implying that the increased resistance of the boundary layers affects the influence coefficients about equally.

The influence coefficients associated with both Faraday current and anode leakage current were measured for slagging conditions during test SEG-13. These values, normalized by the inferred plasma resistance of 63 ohms, are presented in Table 4. The parameter α was chosen to give the best (most symmetric) fit to the data; the value associated with Faraday current is $\alpha = 1.4$, while that associated with anode leakage current is $\alpha = 5.1$. The larger value for the latter case reflects the stronger influence of the resistive boundary layer on the leakage current associated coefficients as compared to those induced by the transverse Faraday current. This effect is further demonstrated by comparing the experimental values in Table 4 with the constant conductivity case shown in Table 1. The experimental values for the coefficients induced by leakage ($\hat{Z}^{FA}_{\ell}$ and $\hat{Z}^{AA}_{\ell}$) are considerably larger than for the constant conductivity solution.

Table 4

Measured Influence Coefficients
for Test SEG-13

Index ℓ	$\hat{Z}^{FF}_{\ell}$	$\hat{Z}^{AF}_{\ell}$	$\hat{Z}^{CF}_{\ell}$	$\hat{Z}^{FA}_{\ell}$	$\hat{Z}^{AA}_{\ell}$	$\hat{Z}^{CA}_{\ell}$
-3	.033	.020	-.009			
-2	.079	.051	-.019	-.022	.049	-.001
-1	.145	.095	-.095	-.062	.318	-.002
0	.331	-.095	.095	-.318	-.700	-.009
1	.134	-.032	.025	.318	.318	-.003
2	.079	-.019	.004	.049	.032	-.0005
3	.054			.015	.008	
4	.038			.007		
		$\alpha = 1.4$		$\alpha = 5.1$		

Slag Polarization Experiments

Internal leakage due to slag polarization was determined by measuring the AC resistance between adjacent electrodes. The AC resistnce instrument (described earlier in reference 8), is now a special case of the AC influence coefficient instrument in which R^{AA}_{k-k} and R^{CC}_{k-k} are the axial resistances between the k-th and (k+1)-th anodes and cathodes, respectively. With the improved version of the AC diagnostic instrument, axial resistances as low as 0.1 ohms can be resolved. The AC resistance instrument measures the parallel combination of the slag layer resistance and the "axial plasma" resistance which is given by the appropriate zeroth influence coefficient. Interpretation of the AC resistance measurement requires a comparison with the "normal" value. In practice, slag layer polarization effects are so strong[8] that this relative comparison is obvious.

The time constant for polarization was determined in the present SEG-13 experiment by measuring the axial resistances as a function of time for various levels of current. The polarization experiment was repeated by reversing the direction of the magnetic field (and hance the electrode polarity). Since the slag layer polarization is caused by the transfer of ionic species (mainly Fe^{++} and K^{+})[9] through the slag, the degree of polarization should depend on net ionic charge transport instead of time alone. This supposition is tested by plotting the axial resistance data versus the parameter, $I_F t$, a measure of net charge transferred. The dependence of axial resistance on $I_F t$ is shown in Figs. 13 and 14 for two levels of Faraday current and opposite channel polarity. Note that the slag layer axial resistance increases at the anodes and decreases at the cathodes with time. The polarized levels of axial resistance depend on the Faraday current for both anodes and cathodes, with larger axial resistances attained at the lower levels of Faraday current.

The axial resistance data of Figs. 13 and 14 were fitted to an exponential decay law of the form:

$$\frac{RX - RX_i}{RX_\infty - RX_i} = 1 - \exp\left(-I_F t/\tau_Q\right) \qquad (18)$$

where RX_i and RX_∞ are, respectively, the initial and the final values of axial resistance and τ_Q is a charge "time constant". As shown in Figs. 13 and 14, the exponential decay law fits the data well for τ_Q = 7.5 - 7.7 amp-minutes over a factor of 4.4 change in current level.

The depolarization of the anode versus the cathode slag layers followed by polarization in the opposite direction was observed during subsequent electrical loading experiments as shown by Figs. 15a and 15b. Despite the interruption and changes in Faraday current, the opposing polarization effects at anodes versus cathodes is well demonstrated.

The results of the present experiment indicate that quite low axial resistances are realized at the cathodes for a core current density of 0.83 amps/cm^2. This low cathode axial resistance can be generalized to other insulator widths by the relation:

$$RX^C = 2.9/w \quad (\Omega) \qquad (19)$$

where w is in cm. The time required to reach 99 percent of this polarization is:

$$t_{99} = 6.9/J_F \quad (\text{min}) \qquad (20)$$

where J_F is in (amp/cm^2). These values for RX^C and t_{99} are probably a function of coal type as well as electrode temperature.

Experiments with Externally Applied Faults

The electrical characteristics of interelectrode faults were investigated by introducing external resistances between adjacent electrodes.

Clean Fuel Experiment. A preliminary leakage experiment was conducted on the clean fuel M-2 channel at a mass flowrate of 0.1 kg/sec and N_2/O_2 = 0. These flow parameters resulted in a core velocity of 370 m/sec and a plasma conductivity (measured by voltage probes) of 11 mho/m. The generator operation in the uniform mode can be characterized by a constant voltage drop of 65 volts and a plasma resistance of 14 ohms which corresponds to an effective conductivity of 6 mhos/m. The Hall voltage performance, as characterized by the α parameter (= $\langle V_H\rangle/\langle I_F\rangle$) decreased in a nonlinear fashion as the transverse current density was increased (see Fig. 16). Note that the experimental data approach the calculated value of α (based on measured core conductivity) for low current densities.

A variable leakage resistance was inserted between the #7 and #8 anodes. The V-I characteristic for this leakage current, i_7^a, and the corresponding Hall voltage, V_{H7}^a, is shown in Fig. 17 along with the neighboring Hall voltages. As the anode gap at #7-8 is shorted, the Hall voltage across the adjacent gaps increased by about 40 percent. The nonshorted Hall voltage was 32 volts and the short circuit gap current was 8.5 amps which corresponds to a maximum fault power of about 70 watts.

The Faraday currents at electrodes #6, 7, and 8 are shown in Fig. 18. The currents associated with the shorted gap (#7 and #8) show small linear changes in opposite directions as the leakage current is increased. The other Faraday currents, such as I_6, were not noticeably changed.

Neglecting the small variations in the Faraday currents, the maximum leakage current can be related directly to the Z_0^{AA} influence coefficient by:

$$Z_0^{AA} = -\frac{V_{H7}^a|_{O.C.}}{i_7^a|_{S.C.}} \qquad (21)$$

For the present experiment, Z_0^{AA} = - 3.8 Ω or $\hat{Z}_0^{AA}$ = - 0.27.

Slagging Experiments. The 120's run series of the SEG-13 experiment, in which an externally aplied axial resistance was decremented between runs, shows the effect of interelectrode resistance on Hall voltage (Fig. 19a). While interelectrode resistances of 80 Ω have negligible effect on Hall voltage, substantial leakage occurs at values of 20 Ω and the Hall voltage approaches zero when interelectrode resistance reaches 5 Ω. These results indicate that the critical value of interelectrode resistance for the initiation of Hall voltage degradation is around 50 Ω.

Figure 19b shows the effect on Hall voltages of an externally applied short coupled with a downstream low current perturbation. The low Faraday current tends to decrease the upstream anode Hall voltages and increase the downstream anode Hall voltages in accordance with the Hall effect. As the externally applied axial resistance is reduced, it forces the corresponding Hall voltage to zero and, in addition, reduces the effect of the low current perturbation on the downstream Hall voltages. Note, however, that the effect of the current perturbation on upstream Hall voltages increases with decreasing resistance (i.e., upstream Hall voltages decrease). Thus the influence of the current perturbation is transferred upstream.

Figure 19c shows the effect on Hall voltages of a low current perturbation just upstream of an externally applied short. Here, as the applied resistance decreases, it forces the corresponding Hall voltage to zero and reduces the effect of the current perturbation on upstream Hall voltages. The effect of the current perturbation on Hall voltages downstream of the short augments as resistance decreases, thus the influence of the current perturbation is transferred downstream.

The initiation of Hall voltage degradation occurs at higher values of interelectrode resistance when multiple faults are involved (Fig. 20). For multiple faults of equal axial resistance, the downstream-most Hall voltage decreases first.

Comparison of Computer Model with Experiment

In using the computer code which solves for the Faraday and leakage currents as functions of time as specified by Eqs. (10), (11), and (12), various arc voltage characteristics for warm mild steel electrodes were employed (Fig. 21) to simulate channel operation in upolarized and polarized states. Figure 22 shows the computer code predictions for the effect of externally applied shorts for the following cases: 1) unpolarized channel, 2) polarized channel, but with no shorting between cathodes, 3) polarized channel with 5 Ω shorts between cathodes, and 4) polarized channel with 2 Ω shorts between cathodes. The results agree qualitatively with the results of the 120 run series of SEG-13 (Fig. 22a). Cathode polarization has the effect of reducing the anode Hall voltages at lower levels of leakage (higher R^a). Figure 23 shows the effect of multiple externally applied shorts for the same four channel operating conditions. The presence of multiple shorts reduces the anode Hall voltages at lower levels of leakage than for the single short case. This effect is further augmented when the cathodes are polarized. Again these results agree qualitatively with the results of the 160 run series of SEG-13 (Fig. 23).

Figure 24 shows the steady state Faraday currents obtained in SEG-13 for two different loadings along with the predictions of the computer code. For the channels in the polarized conditions with 5 Ω shorts between cathodes, the numerical results agree fairly well with the SEG-13 experiment. Note the code accurately predicts the end effects.

Results of the 120 run series of the SEG-13 experiment yield an open circuit Hall voltage of 18 volts and a short circuit gap current of 1.2 amps (Fig. 25) when the channel was uniformly loaded ($\langle I_F \rangle = 4.5$ amps); this corresponds to a maximum fault power of 5.4 watts. An upstream low current perturbation significantly increased this value to 36 watts. Numerical results indicate the same trends (Fig. 25); downstream high and upstream low Faraday currents tend to increase the maximum fault power across a gap while downstream low and upstream high Faraday current perturbations have the opposite effect.

As in the clean fuel case, neglecting channel nonuniformities, the maximum leakage current can be related to the $\hat{Z}_0^{AA}$ influence coefficient by Eq. (21). For the SEG-13 experiment $\hat{Z}_0^{AA}$ is -.30.

IV. Conclusions

Generator electrical nonuniformities were investigated by using the concept of "influence coefficients". This approach allowed the computation of the nonuniform time dependent behavior of a large number of electrodes including the effects of nonlinear voltage drops and leakage resistances. Buckling-type instabilities in axial electrical distributions were calculated and correlated as a function of voltage drop and load resistance. The dependence of maximum fault power on adjacent nonuniformities was shown.

An AC diagnostic instrument was developed and used for the *in situ* measurement of influence coefficients and of axial resistance. The normalized transverse influence coefficients were in excellent agreement with those obtained from a constant conductivity model. Axial influence coefficients depend on the plasma boundary layer and further work on a variable conductivity model is needed. Slag layer polarization was correlated with the charge transferred and a charge "time constant" was determined.

Channel experiments with externally applied axial resistances were conducted for both clean fuel and for slagging conditions. Critical values of axial resistance for Hall voltage degradation were determined as well as maximum fault power. The experimental trends for Hall voltage and leakage current behavior are in agreement with those predicted by the influence coefficient model. Further work on the effects of plasma property variations on the influence coefficient model is in progress.

Acknowledgments

The authors thank Ragui Assaad and Peter Mackreth for their work on the AC diagnostic instrument; and Frank Levy, Bob Conley, Ken Sartain, David Akiyama and Don Munro for their help on the channel hardware and tests.

References

1. Koester, J. K. and Nelson, R. M., "Electrical Characteristics of an Arc-Mode Slagging Electrode Generator," 18th Symposium on Engineering Aspects of MHD, Butte, Montana, June 1979.

2. Demirjian, A., et al., "Long Duration Channel Development and Testing," 18th Symposium on Engineering Aspects of MHD, Butte, Montana, June 1979.

3. Rudins, G., et al., "A Study of the Operation of the U-25B Facility MHD Generator Under Conditions of Strong Electric and Magnetic Fields," 7th International Conference on MHD Electrical Power Generation, Cambridge, Massachusetts, June 1980.

4. Lowenstein, A., "Consolidation and Local Control of Power in an MHD Generator," 17th Symposium on Engineering Aspects of MHD, Stanford, California, March 1978.

5. Solbes, A. and Lowenstein, A., "Electrical Nonuniformities and Their Control in Linear MHD Channels," 15th Symposium on Engineering Aspects of MHD, Philadelphia, Pennsylvania, May 1976.

6. Kuo, S., et al., "Electrical Nonuniformities in Diagonally Connected Generators," Journal of Energy, Vol. 4, No. 2, March-April 1980.

7. Rosa, R. J., Magnetohydrodynamic Energy Conversion, McGraw-Hill, New York, 1968.

8. Koester, J. K. and Nelson, R. M., "Discharging Characteristics of Slagging Metal Electrodes," 17th Symposium on Engineering Aspects of MHD, Stanford, California, March 1978.

9. Koester, J. K. and Perkins, R. A., "Discharge and Corrosion Characteristics of Slagging Metal Electrodes for MHD Power Generators," J. Materials for Energy Systems, Vol. 1, No. 2, pp. 41-54, September, 1979.

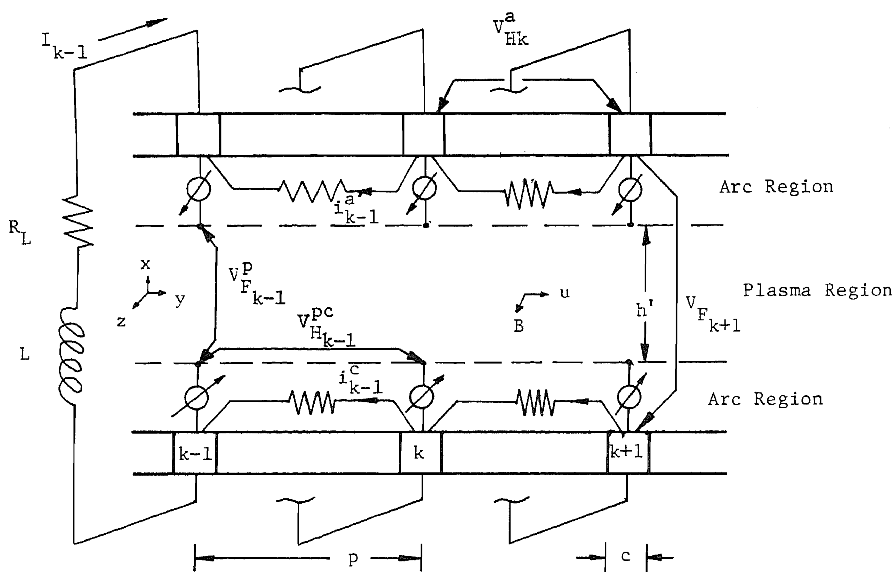

Fig. 1. Schematic of circuit model for segmented Faraday channel with arcs and leakage paths.

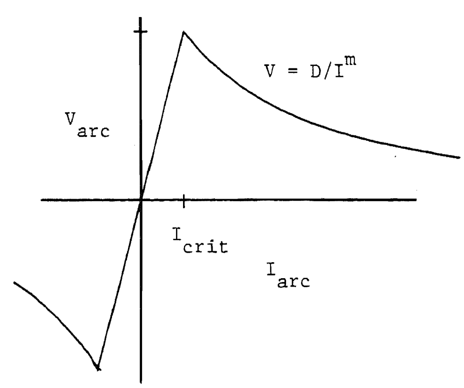

Fig. 2 Voltage-current characteristic for arc model.

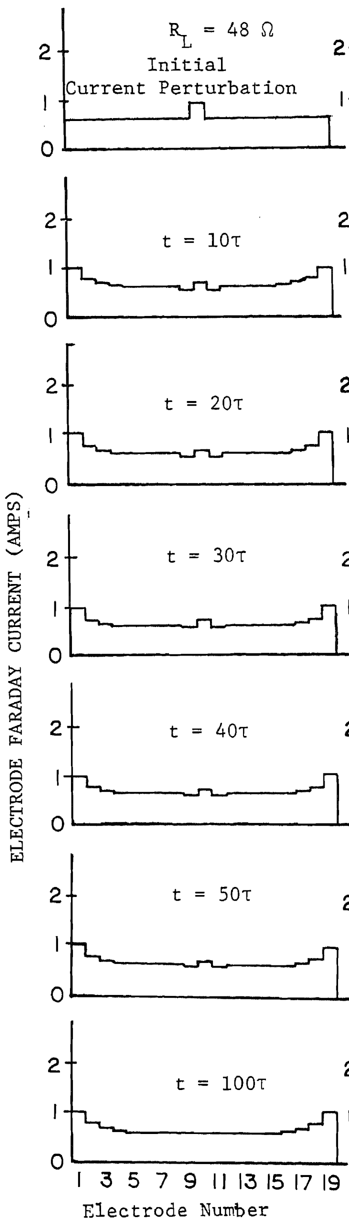

Fig. 3 Current stabilization after an initial current perturbation.

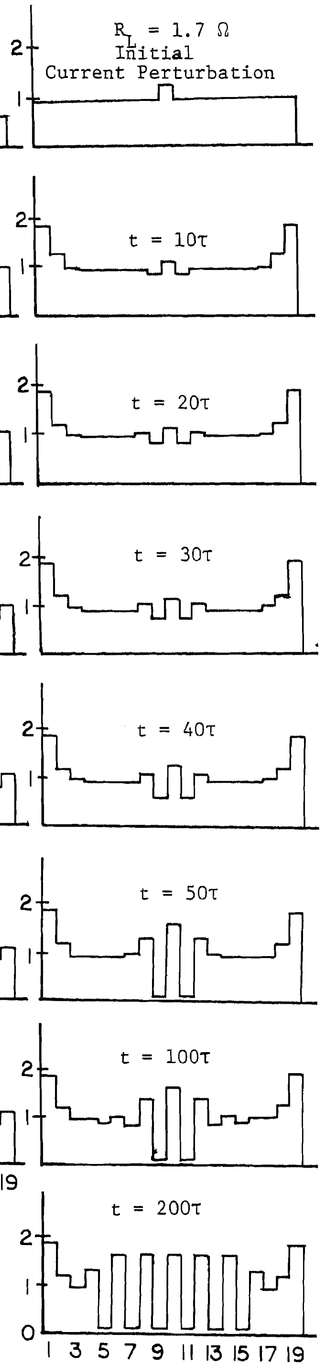

Fig. 4 Growth and spread of instabilities after an initial current perturbation.

For Figs. 3 and 4:

p/h=0.156	c/h=0.010
N =19	R_{ch}=120Ω
V_o =340V	τ =.833μsec
m =.25	D =194 v-a$^{.25}$
I_c =0.11a	

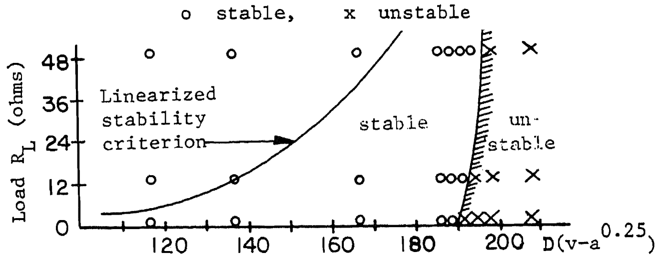

Fig. 5 Stability map showing the effects at external load R_L and voltage drop level D.

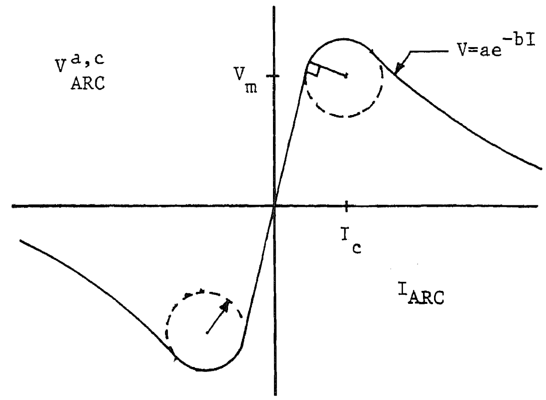

Fig. 6 Arc voltage-current characteristic model employing a decaying exponential.

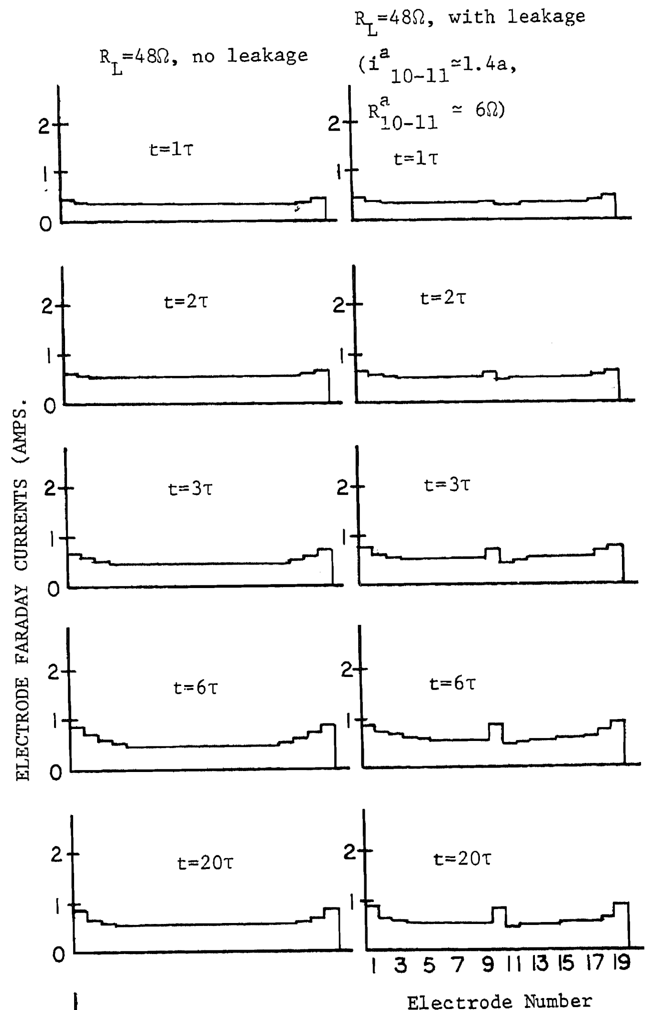

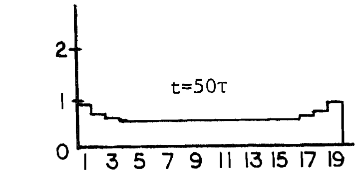

For Fig. 7:

All currents initially zero

p/h=0.156	c/h=0.010
N =19	R_{ch}=120Ω
V_o =340v	τ =.833μsec
V_m =128v	I_c =0.1a
β =1.5	

Fig. 7 Temporal evolution of Faraday currents with and without leakage at high external loads.

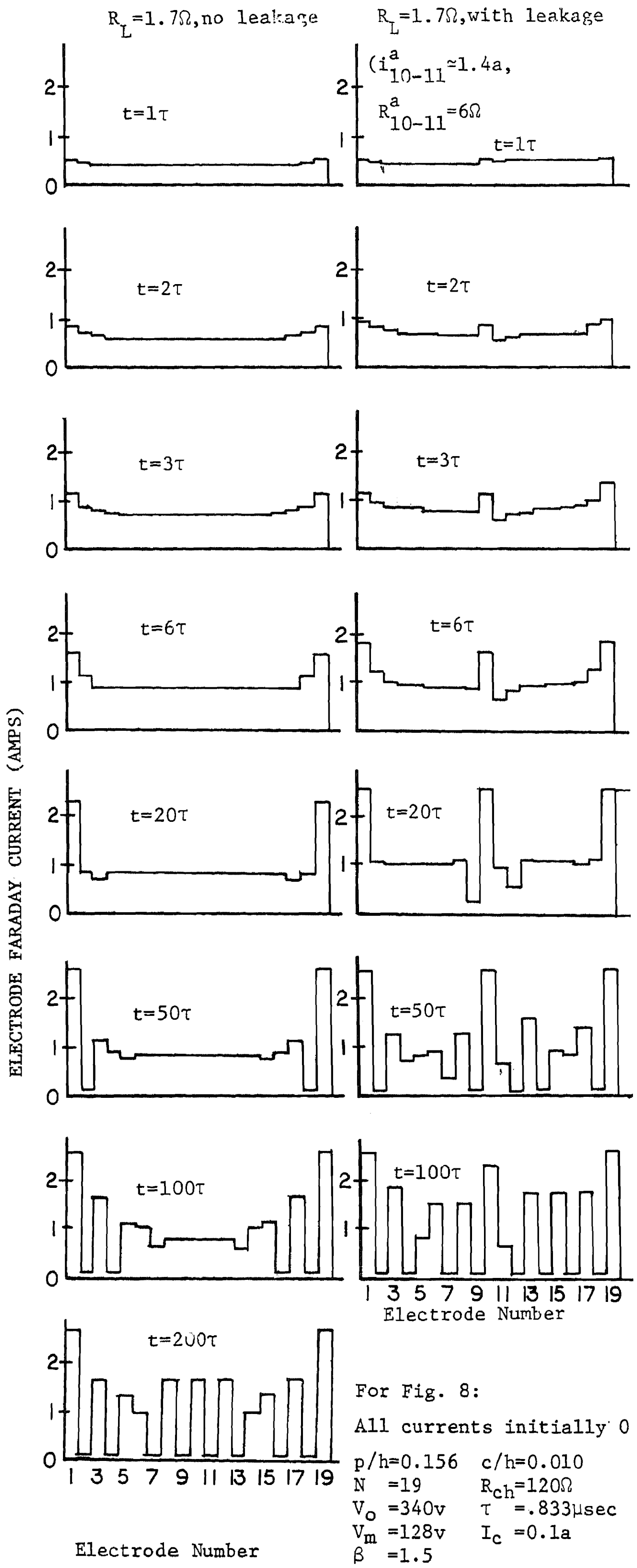

For Fig. 8:

All currents initially 0

p/h=0.156 c/h=0.010
N =19 R_{ch}=120Ω
V_o =340v τ =.833μsec
V_m =128v I_c =0.1a
β =1.5

Fig. 8 Temporal evolution of Faraday currents with and without leakage at low external loads.

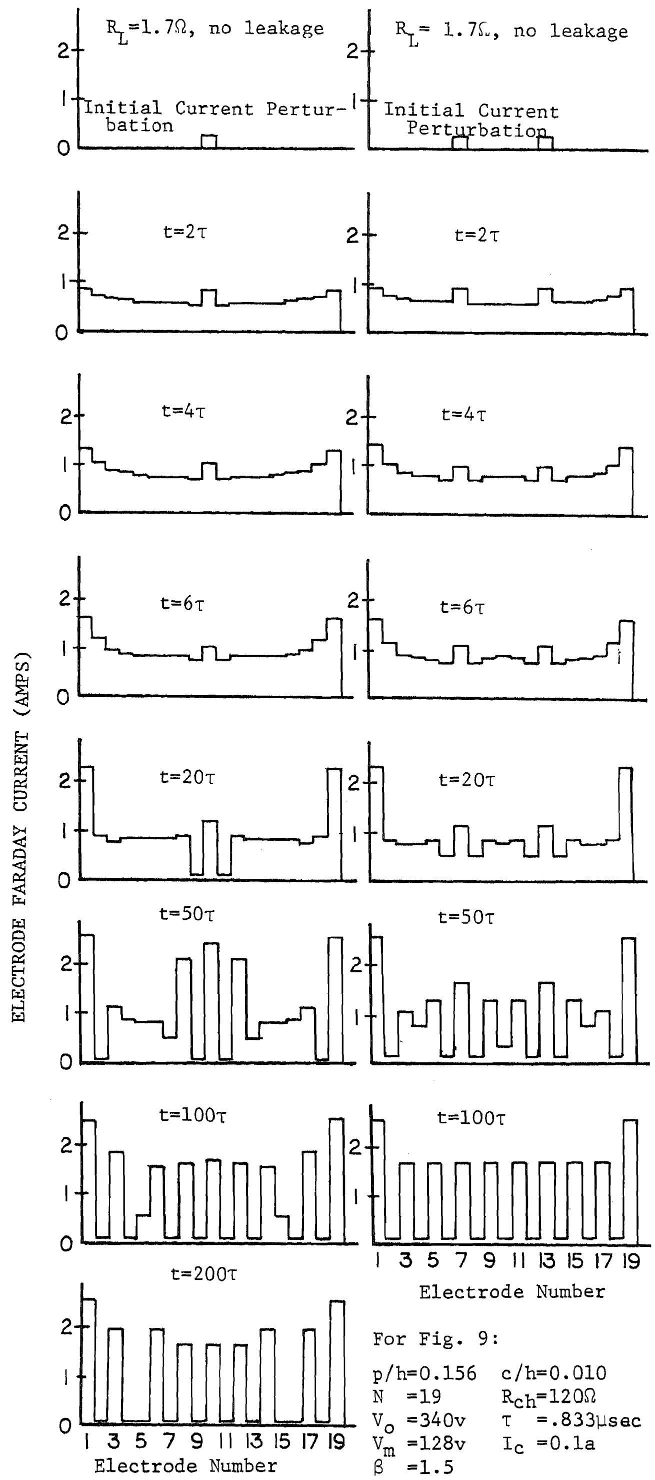

For Fig. 9:

p/h=0.156 c/h=0.010
N =19 R_{ch}=120Ω
V_o =340v τ =.833μsec
V_m =128v I_c =0.1a
β =1.5

Fig. 9 Effect of initial current perturbations on the development of buckling-type instabilities.

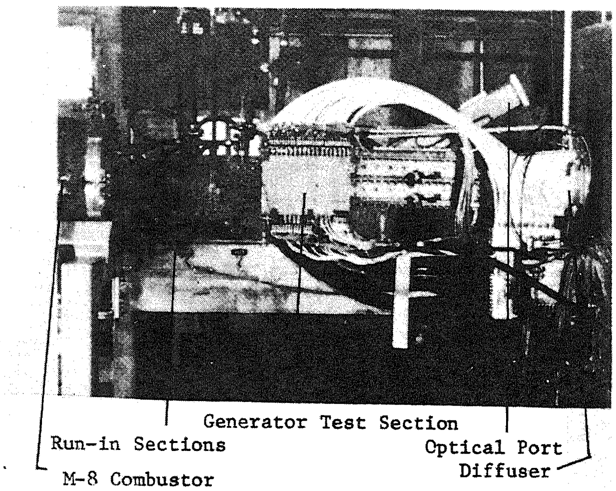

Fig. 10 Slagging electrode generator flowtrain.

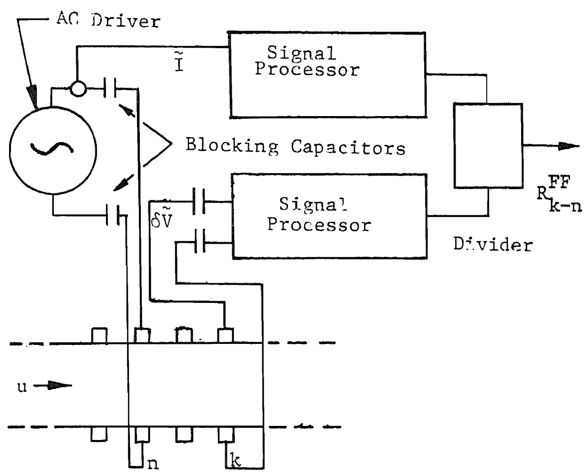

Fig. 11 Schematic of the AC influence coefficient instrument.

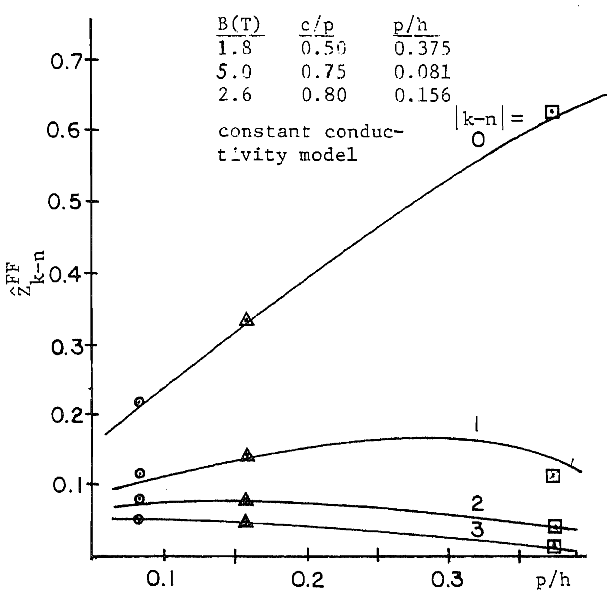

Fig. 12 Normalized influence coefficients versus pitch/height ratio for two channels compared with constant conductivity model.

For Figs. 13-15:
△ Anode open-top
o Cathode closed-bottom

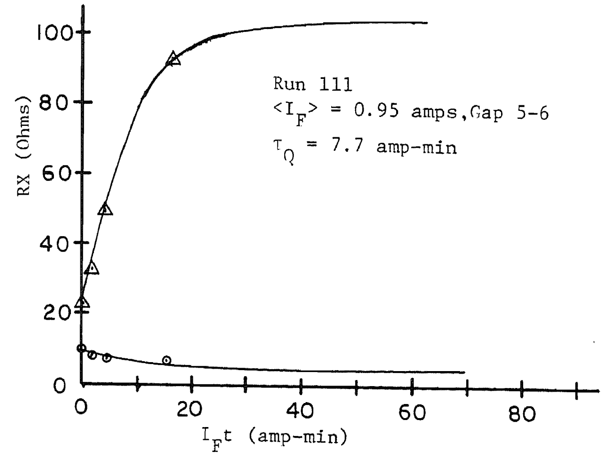

Fig. 13. Axial resistance versus charge transfer parameter.

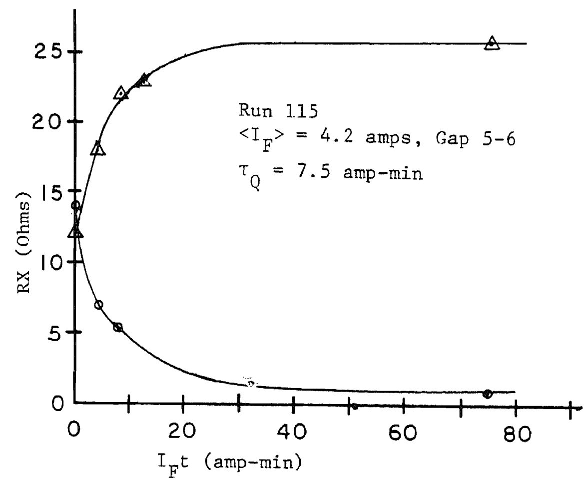

Fig. 14. Axial resistance versus charge transfer parameter.

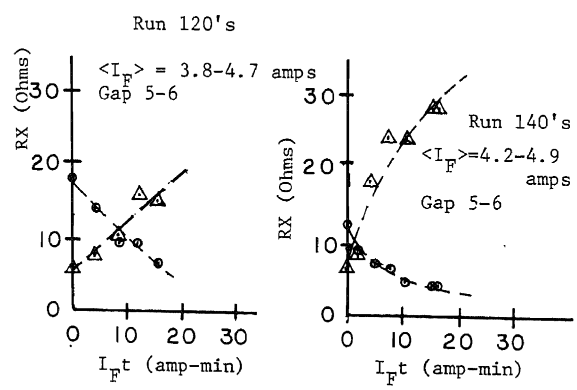

Fig. 15. Axial resistance versus charge transfer parameter.

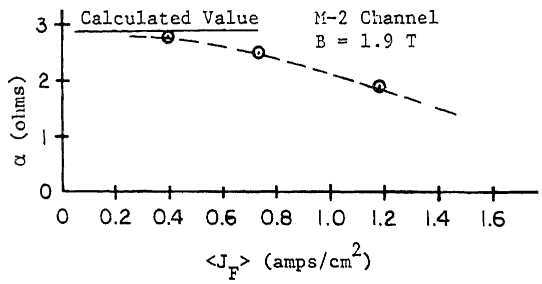

Fig. 16 Hall voltage parameter versus average transverse current density.

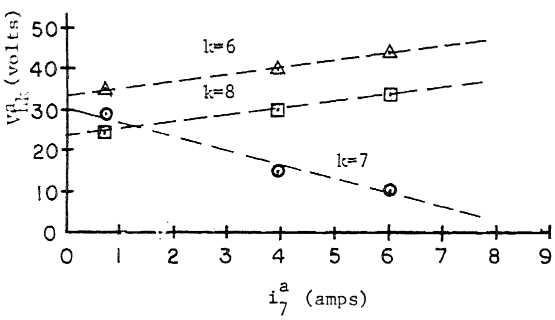

Fig. 17 Anode Hall voltage versus leakage current.

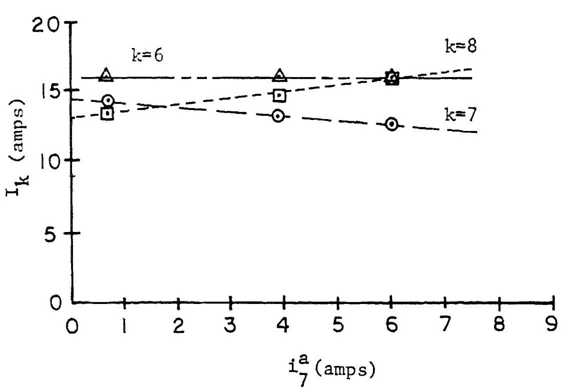

Fig. 18 Faraday current versus leakage current.

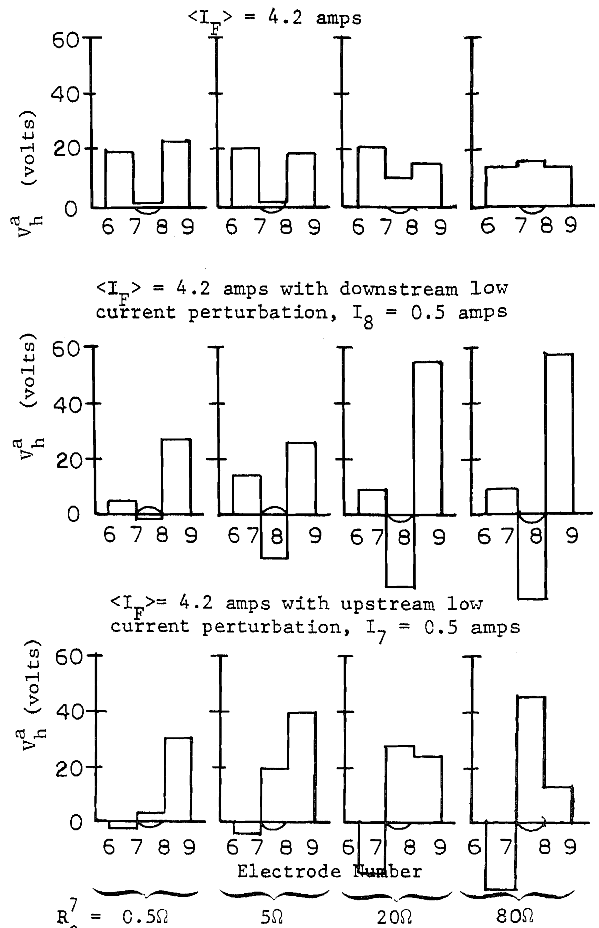

Fig. 19a,b,c Influence of an externally applied short on anode Hall voltages.

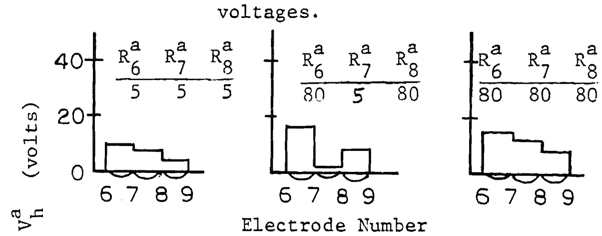

Fig. 20 Influence of multiple applied shorts on anode Hall voltages.

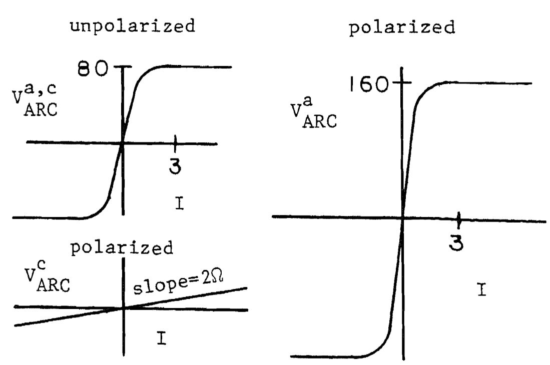

Fig. 21. Arc voltage-current characteristic model for warm mild steel electrodes.

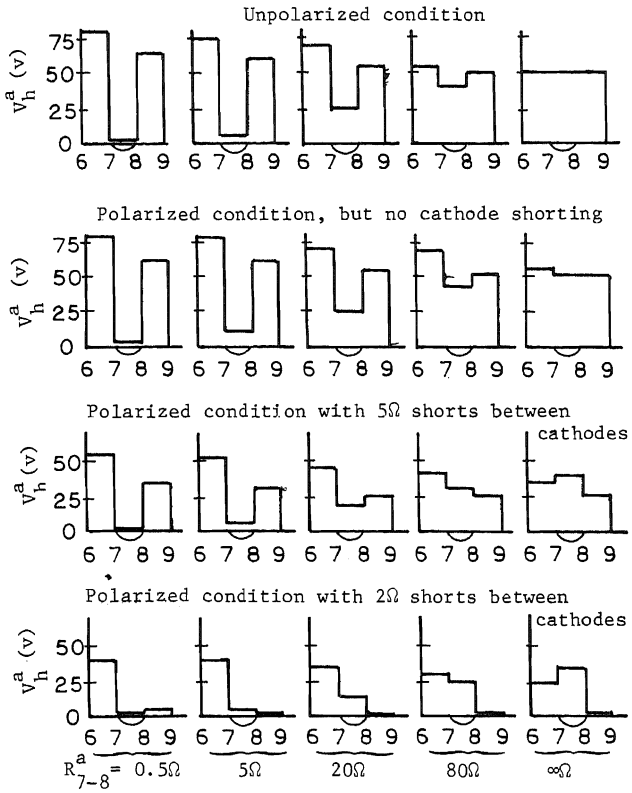

Fig. 22 a,b,c,d Computer predictions of the influence of an externally applied short on Hall voltages under the conditions of the SEG 13 experiment

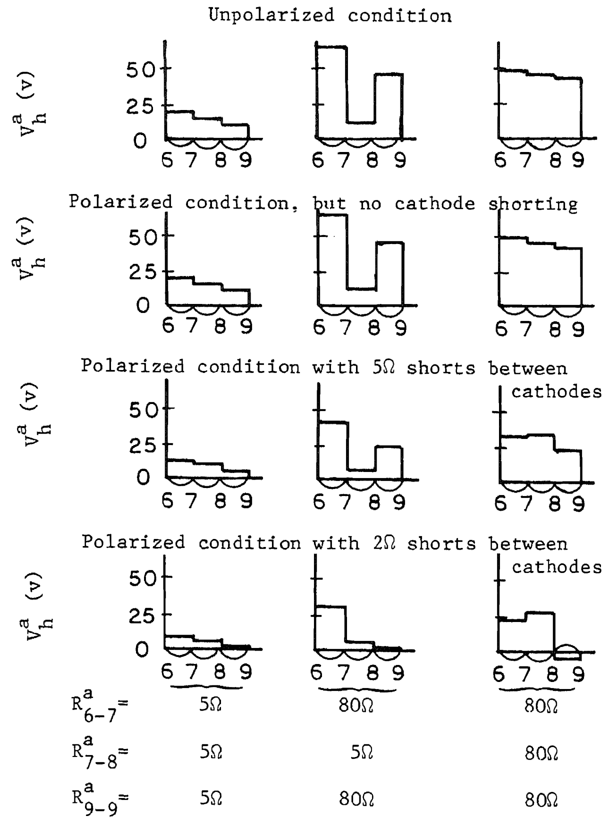

Fig. 23. Computer predictions of the influence of multiple externally applied shorts on Hall voltages under conditions of the SEG 13 experiment.

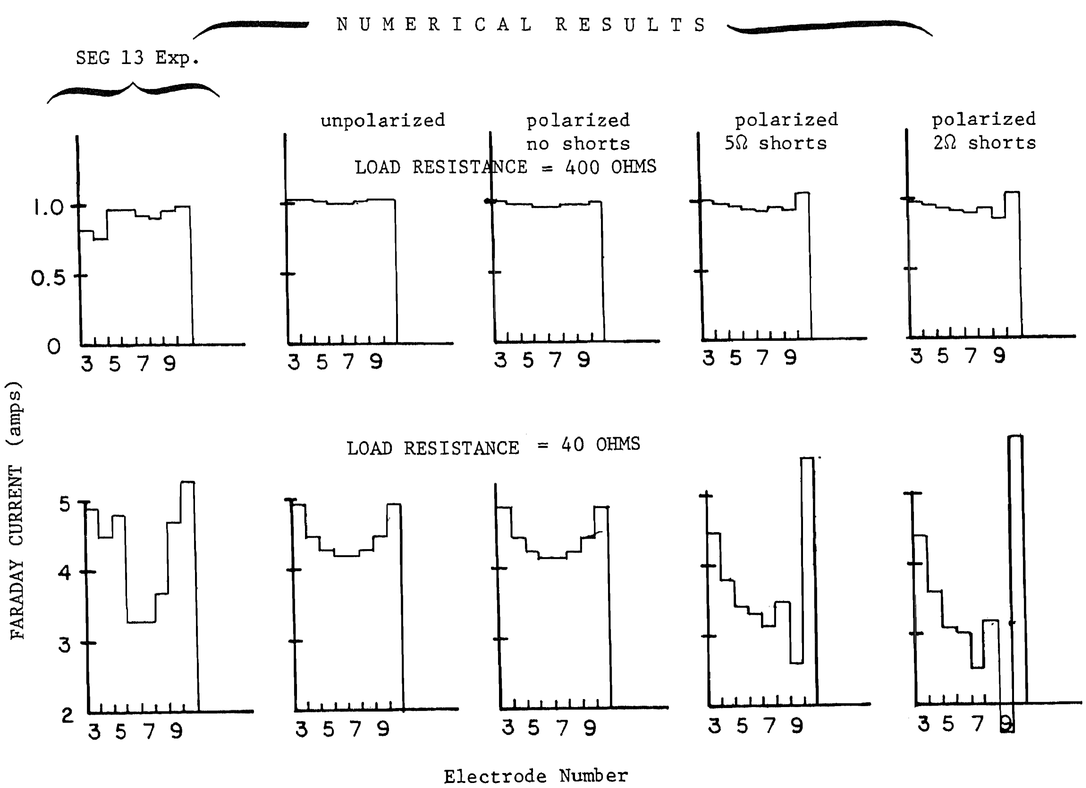

Fig. 24. Experimental and analytical steady state Faraday currents (operating electrodes #3 - 10).

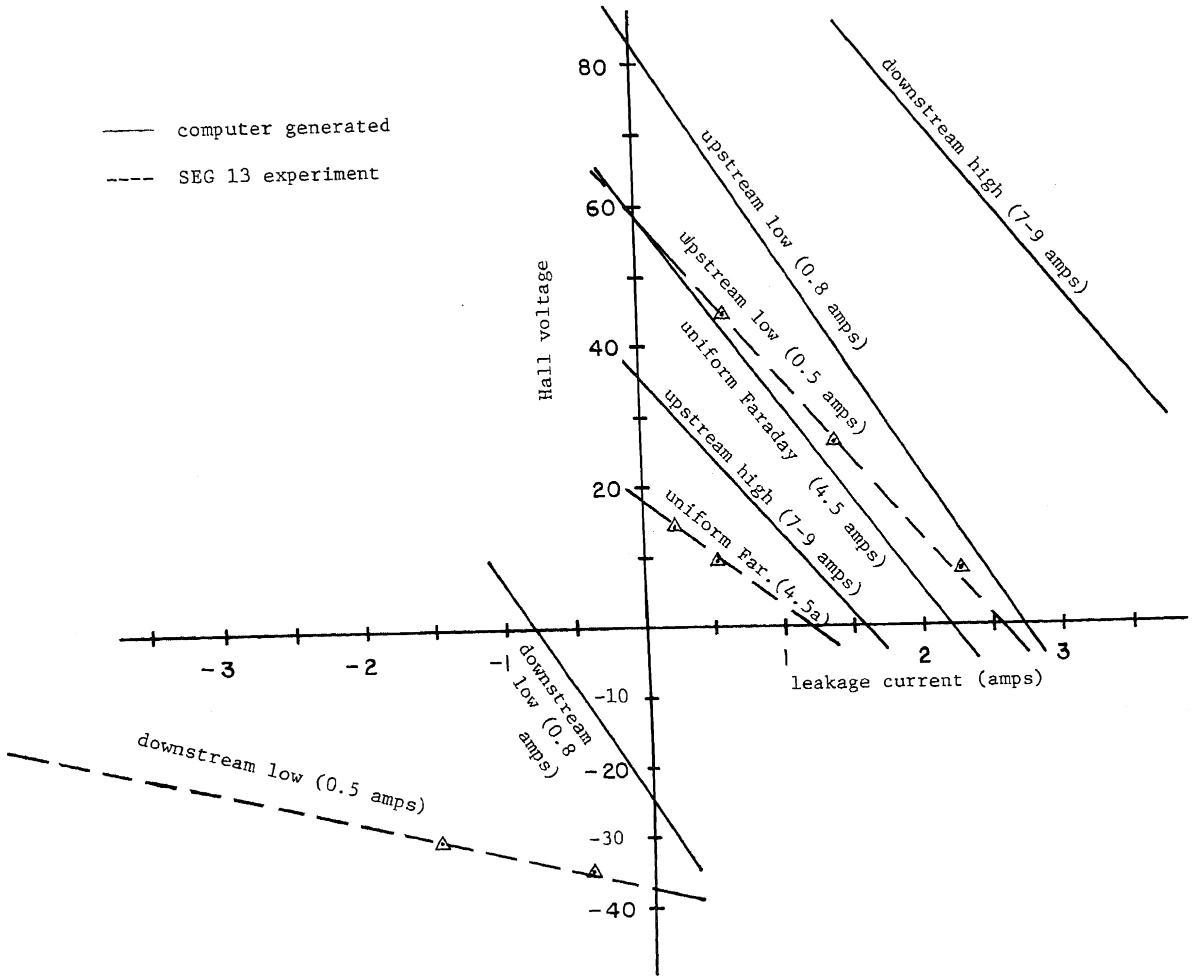

Fig. 25. Effect of Faraday current perturbations on Hall voltage-leakage current characteristics.